Paclitaxel-loaded chitosan oligosaccharide-stabilized gold nanoparticles as novel agents for drug delivery and photoacoustic imaging of cancer cells

Panchanathan Manivasagan[a], Subramaniyan Bharathiraja[a], Nhat Quang Bui[b], In Gweon Lim[c], Junghwan Oh[a,b,*]

[a] Marine-Integrated Bionics Research Center, Pukyong National University, Busan 608-737, Republic of Korea
[b] Department of Biomedical Engineering and Center for Marine-Integrated Biotechnology (BK21 Plus), Pukyong National University, Busan 608-737, Republic of Korea
[c] Department of Mechanical Engineering, Myong-Ji University, San 38-2, Nam-dong, Cheoin-gu, Yongin-si, Gyeonggi-do 449-728, Republic of Korea

ABSTRACT

Polymer nanoparticles have gained significant attention as potential drug carriers for anticancer agents and molecular imaging. Biocompatible gold nanoparticles (AuNPs) were synthesized using chitosan oligosaccharide (COS) as a reducing and stabilizing agent and were subsequently loaded with paclitaxel (PTX) to demonstrate their use in drug delivery and photoacoustic imaging (PAI) of MDA-MB-231 cells. Paclitaxel-loaded chitosan oligosaccharide-stabilized gold nanoparticles (PTX-COS AuNPs) were spherical in shape with an average particle size of 61.86 ± 3.01 nm. PTX-COS AuNPs showed sustained and pH-dependent drug release profiles and exhibited strong cytotoxic effect against MDA-MB-231 cells through the induction of apoptosis with improved reactive oxygen species (ROS) generation and altered mitochondrial membrane potential (MMP) level. The cellular internalization of PTX-COS AuNPs was proven by fluorescence microscopy as well as flow cytometry. PTX-COS AuNPs were also evaluated as a new class of optical contrast agents for photoacoustic imaging (PAI). To the best of our knowledge, this is the first report that describes the use of PTX-COS AuNPs as novel agents for drug delivery and PAI of cancer cells. These results exposed the promising potential of PTX-COS AuNPs in the field of drug delivery, molecular imaging, and cancer therapy in the near future.

© 2016 Published by Elsevier B.V.

1. Introduction

Nanotechnology has immense potential to revolutionize biomedical research with the development of novel and improved nano-products for clinical diagnosis and therapy (Krishnaraj et al., 2014). Polymer nanoparticles have emerged as potential drug carriers for anticancer agents and molecular imaging (Venkatpurwar et al., 2011; Choi et al., 2012). Chitosan (CS), a natural biopolymer, has emerged as an attractive biomaterial for drug-delivery systems because of its biocompatible, biodegradable, and nontoxic nature (Kumar et al., 2004; Xue et al., 2015). However, the main problem of CS is its poor solubility at neutral pH. Chitosan oligosaccharide (COS), a water-soluble hydrophilic backbone (Hu et al., 2008), was developed to overcome these problems and serve as an excellent candidate for drug delivery (Liu et al., 2008). COS has outstanding advantages compared with chitin and CS. COS, a low molecular weight depolymerization product of CS, has recently received considerable attention in biomedical applications because of its low-cost, water-soluble, abundant, biocompatible, biodegradable, and nontoxic nature. In addition, it possesses unique bioactivities, including antimicrobial, antitumor, and antiviral activities (Manivasagan and Oh, 2016). COS is mainly suitable for polymer-drug conjugates because of its accessibility for coupling with the primary amino groups and hydroxyl groups of each polymer subunit and the cationic nature that allows ionic crosslinking (Agnihotri et al., 2004). COS has been improved with hydrophobic residues, including cholesterol, deoxycholic acid,

tocopherol, and alkyl groups. This hydrophobically improved COS can form self-assembled nanoparticles, which can be used as carriers for gene and tumor-targeted drug delivery (Chae et al., 2005).

Carbon nanomaterials such as carbon nanotubes and graphene are being constantly researched to explore their applications (De Volder et al., 2013). Carbon nanotubes and graphene are both low-dimensional sp^2 carbon nanomaterials displaying several unique properties that are interesting in a broad range of applications such as drug delivery, imaging, and nanomedicine (Kruss et al., 2013). Since 2004, carbon nanotubes have been used as delivery carriers. *In vivo* cancer treatment with carbon nanotubes has been established in animal experiments by various groups (Liu et al., 2011). Recently, graphene has also shown promise in several biomedical applications. Graphene has been extensively explored as drug delivery and cancer treatment. However, the major drawback of carbon nanomaterials are limited solubility, extremely small, expensive, poor distribution among cells, inability of drugs to cross cellular barriers, (Heister et al., 2009) and particularly a lack of clinical procedures for overcoming multidrug resistant cancer (Jabr-Milane et al., 2008), all limit the clinical administration of chemotherapeutic agents. In recent years, these problems are subject to intensive research worldwide. In this context, a broad range of various types of drug delivery systems have been investigated, including polymers, silica nanoparticles, quantum dots and liposomes. Gold nanoparticles (AuNPs) have emerged as promising agents for drug delivery, therapy, and diagnosis because of their unique physicochemical properties, including surface plasmon resonance (SPR), optical property, and the capability to permit surface modification for further use in biomedical applications (Huang et al., 2007; Manivasagan et al., 2016). Considering the importance of AuNPs, the study focuses on the biosynthesis these nanoparticles in a green way (Singh et al., 2016). Green synthesis does not involve the use of any toxic chemicals, it is environment-friendly, cost-effective, zero energy based and less time-consuming process (Dhand et al., 2016; Manivasagan et al., 2016). Various marine biopolymers like COS is used as sources under 'green synthesis'. Chitosan oligosaccharide-stabilized gold nanoparticles (COS AuNPs) synthesized by the green process and highly biocompatible with pharmaceutical and other biomedical applications (Tagad et al., 2013).

Paclitaxel (PTX) is one of the successful anticancer drugs used to treat breast and ovarian cancers but has poor solubility and low therapeutic applications (Lee et al., 2008; Tao et al., 2012). Recently, various drug-delivery vehicles, including polymer nanoparticles (Zhang et al., 2005; Zhang et al., 2008) and liposomes (Xiong et al., 2011) were investigated to increase the solubility of PTX and to avoid the side effects, and among these novel drug-delivery systems, polymer nanoparticles have received a greater interest. Human breast cancer is the second most common cause of cancer deaths in women and is increasingly observed in developing and developed countries (Hsieh et al., 2005; Krishnaraj et al., 2014). The existing cytotoxic compounds used for breast cancer treatment are found to be considerably costly, ineffective and may further induce side effects. To overcome this difficulty, the development of efficient novel drug carriers without any side effects is an urgent need (Nagajyothi et al., 2016). Photoacoustic imaging (PAI) is an emerging technology that allows for the imaging of tissues and cells using contrast agents such as nanoparticles. PTX-COS AuNPs have been used as contrast agents for PAI with photoacoustic tomography (PAT) *in vitro*. The aim of the present study is to evaluate the potential of PTX-COS AuNPs as novel agents for drug delivery and PAI of cancer cells.

2. Materials and methods

2.1. Materials

COS (average molecular weight above 10 kDa) was obtained from Kitto Life Co., Ltd. (Seoul, South Korea). PTX, gold (III) chloride trihydrate ($HAuCl_4 \cdot 3H_2O$), 3-(4,5-dimethylthiazol-2-yl)-2,5-diphenyltetrazolium bromide (MTT), acridine orange (AO), ethidium bromide (EB), propidium iodide (PI), Hoechst 33342, 2', 7'-dichlorodihydrofluorescein-diacetate (DCHF-DA), and rhodamine-123 (Rh-123) were obtained from Sigma–Aldrich Co. (St. Louis, MO, USA). Dimethyl sulfoxide (DMSO) was purchased from Junsei Chemical Co., Ltd (Tokyo, Japan). All chemicals procured from Sigma–Aldrich Co. (St. Louis, MO, USA) were of analytical grade.

2.2. Synthesis of COS AuNPs

COS (0.05 g) was added to 10 mL aqueous solution of 1×10^{-4} M $HAuCl_4 \cdot 3H_2O$, and the solution was kept in magnetic heater stirrer at 80 °C for 1 h, which resulted in a dark ruby red color indicating the formation of AuNPs. The formation of AuNPs was observed with UV–vis spectroscopy using Beckman Coulter DU530 Life Science UV/Vis spectrophotometer (Beckman Coulter, Fullerton, CA, USA). The synthesized AuNPs were collected by centrifugation at $12,000 \times g$ for 30 min, washed many times with deionized water by centrifugation, and re-dispersed in water to remove excess gold. The AuNPs dispersion was dialyzed using a dialysis tube with 12,000 Da molecular weight cutoff for 24 h to remove ionic impurities.

2.3. Preparation of PTX-COS AuNPs

For preparing PTX-COS AuNPs, 20 mg of COS AuNPs was dissolved in 10 mL deionized water, added with 1 mg/mL PTX in DMSO, and kept for 24 h at room temperature to allow proper interaction between the drug and COS AuNPs. The resulting solution was sonicated and centrifuged at 12,000 rpm for 30 min and then dialyzed against deionized water for 12 h. The dialysates were kept at −20 °C until required for further experiments.

To determine the drug loading (DL) efficiency and drug contents (DCs), the samples were freeze-dried and then dissolved in DMSO. The amount of PTX was measured by UV spectrophotometry at 490 nm. The DL efficiency and DCs were calculated by Eqs. (1) and (2), respectively:

$$DL(\%) = \frac{\text{Amount of drug in nanoparticles}}{\text{Amount of drug initially added}} \times 100 \qquad (1)$$

$$DC(\%) = \frac{\text{Amount of drug}}{\text{Amount of drug and polymer}} \times 100 \qquad (2)$$

2.4. Characterization of COS AuNPs and PTX-COS AuNPs

The biosynthesized COS AuNPs were subjected to lyophilization and were powdered for X-ray diffraction (XRD) analysis (X'Pert-MPD, Philips, Almelo, Netherlands). The COS, COS AuNPs, PTX, and PTX-COS AuNPs were freeze dried, powdered, and ground with KBr and analyzed using Fourier transform infrared spectroscopy (FTIR) (Perkin Elmer Inc., USA). FTIR spectra of COS, COS AuNPs, PTX, and PTX-COS AuNPs were recorded using spectrum GX spectrometry in diffuse reflectance mode operated at a resolution of 4 cm^{-1} of wavelength from approximately $4000–400 \text{ cm}^{-1}$. The particle size, morphology, and composition of COS AuNPs and PTX-COS AuNPs were analyzed using field emission scanning electron microscopy

(FESEM; JSM-6700, JEOL, Japan), high-resolution transmission electron microscopy (HRTEM; JEM 2010, JEOL, Japan), and energy dispersive X-ray spectroscopy (EDX). The particle size was determined by dynamic light scattering (DLS) method using electrophoretic light scattering spectrophotometer (ELS-8000, OTSUKA Electronics Co. Ltd., Japan) at a fixed angle of 90° and at room temperature. The zeta potential (ZP) of the COS AuNPs before and after loading PTX was measured with an electrophoretic light scattering spectrophotometer (ELS-8000, OTSUKA Electronics Co. Ltd., Japan) using ELS FlatBoard cell.

2.5. Stability study of COS AuNPs

The stability study of COS AuNPs was performed at room temperature. The change in SPR of the nanoparticle dispersion was observed up to six months using UV–vis spectroscopy. The pH of COS AuNPs (pH 2.0–12.0) was adjusted using 0.1 N HCl and 0.1 M NaOH for decreasing or increasing the pH of water, respectively, using calibrated pH meter. The effect of the electrolyte on COS AuNPs dispersion was recorded at various concentrations of NaCl (10^1 to 10^5 M). The change in SPR was observed after 24 h using UV–vis spectroscopy.

2.6. In vitro drug release studies

In vitro release profile of PTX from COS AuNPs was determined under sink conditions at various pH, i.e., 5.5, 6.8, and 7.4 at 37 °C. PTX-COS AuNPs solution (1 mL) was dialyzed against 10 mL phosphate-buffered saline solution (PBS) and placed in a cellulose acetate membrane (MWCO: 10 000 Da) in a magnetic heater stirrer at 37 °C with continuous stirring at 180 rpm. At predetermined time intervals, all outer solutions were exchanged with fresh PBS solution, and the solution containing released PTX was quantitatively analyzed. The amount of PTX released was analyzed using a spectrophotometer at 490 nm. The experiments were performed in triplicates for each sample.

2.7. In vitro cytotoxicity studies

2.7.1. Cell viability assay

Human breast cancer cell line (MDA-MB-231) was obtained from Korean Cell Line Bank, Seoul, South Korea and maintained in Dulbecco's Modified Eagle Medium (DMEM, HyClone, Logan, UT, USA) and, cultured at 37 °C in a 5% CO_2 atmosphere. The cells were seeded in a 96-well plate at density of 5×10^4 cells/well. The cells were treated with different concentrations of COS, COS AuNPs, PTX, and PTX-COS AuNPs (20, 40, 60, 80, 100, 120, 140, 160, 180, 200, 220, 240, 260, 280, 300, and 320 μg/mL) for 24 h and 48 h. The treated cells were incubated for 24 h and 48 h to analyze cytotoxicity using MTT assay. Then, 100 μL MTT (0.5 mg/mL) was added in each well and incubated for 4 h. The purple color formazan crystals formed were dissolved in 100 μL of DMSO and the absorbance was recorded at 570 nm in a multi-well ELISA plate reader (BioTek, Power Wave XS2, VT, USA). Optical density value was converted to percentage of viability using the following Formula (3):

$$\text{Percentage of cell viability}(\%) = \frac{\text{OD value of samples}}{\text{OD value of controls}} \times 100 \quad (3)$$

2.7.2. Morphological observation

The MDA-MB-231 cells were treated with IC_{50} concentration of PTX-COS AuNPs and incubated for 24 and 48 h in 5% CO_2 atmosphere. After the incubation, the cell morphological changes were viewed under a Leica DMI3000 B inverted phase contrast microscope (Leica Microsystems GmbH, Wetzlar, Germany).

2.7.3. Apoptosis study

The ability of PTX-COS AuNPs to induce apoptosis in MDA-MB-231 cells was confirmed using an acridine orange (AO) and ethidium bromide (EB) (1:1 ratio of AO and EB in PBS) staining method (Karthik et al., 2014) for 24 h and 48 h. The cells collected were washed with PBS and stained by adding 100 μL of AO and EB for 5 min then the excess unbinding dye was removed by washing with PBS. Stained cells were visualized under a fluorescence microscope (Leica Microsystems GmbH, Wetzlar, Germany). The apoptotic cells with the shrunken, fragmented nuclei and brightly fluorescent and EB-positive necrotic cells were scored and the percentage apoptotic cells were determined by the following formula:

$$\% \text{ of apoptotic cells} = \frac{\text{Total number of apoptotic cells}}{\text{Total number of normal and apoptotic cells}} \times 100 \quad (4)$$

MDA-MB-231 cells were plated at a density of 5×10^4 cells/well in a 6-well plate. At >90% confluence, the cells were treated with PTX-COS AuNPs for 24 and 48 h. The cells were washed with PBS and fixed in methanol: acetic acid (3:1 v/v) for 10 min. After fixation, they were stained with 50 μg/mL of PI for 20 min. Nuclear morphology of apoptotic cells were observed under a fluorescence microscope.

Hoechst 33342 stain is a fluorescent dye mostly used to detect the diverse characteristic structures during apoptosis process. MDA-MB-231 cells were treated with IC_{50} concentration of PTX-COS AuNPs for 24 and 48 h. The cells were washed with PBS, fixed in methanol: acetone (3:1, v/v), and stained with Hoechst 33342 (5 μg/mL) at 37 °C for 10 min. Nuclear morphology of apoptotic cells was studied under a fluorescence microscope (Manivasagan et al., 2015).

2.7.4. Reactive oxygen species (ROS) detection

For quantifying the intracellular ROS, the cells were seeded into 6-well plates at a density of 5×10^5 cells/well and incubated for 24 h. After incubation, the cells were treated with fresh medium containing PTX-COS AuNPs and incubated for 24 h and 48 h. After the incubation, the medium was removed and 10 μM of DCHF-DA, a non-fluorescent probe that can penetrate into the intracellular matrix of cells, was added to the cells. It was oxidized by ROS to fluorescent dichlorodihydrofluorescein (DCF), and the cells were then kept in the incubator for 30 min. The cells were washed with PBS to remove the excess dye and further observed and imaged with a fluorescence microscope.

2.7.5. Mitochondrial membrane potential

Mitochondrial membrane potential (MMP) was assessed following the procedure described by Bhosle et al. (2005) using Rh-123, which is a lipophilic cationic dye, highly specific for mitochondria. The cells were seeded in a 6-well plate and treated with PTX-COS AuNPs and incubated for 24 h and 48 h. After incubation of the cells, fluorescent dye Rh-123 (10 μg/mL) was added in each cells and further incubated for 30 min after which the cells were washed with PBS and observed under a fluorescence microscope.

2.8. Cell cycle analysis

Cell cycle distribution and percentage of apoptotic cells were analyzed by flow cytometry (Tai et al., 2000). After treatment, the floating cells in the medium were combined with attached cells collected by trypsinization. The cells were washed with cold PBS and fixed with ice-cold 80% ethanol in PBS at −20 °C. They were allowed to stand overnight, and cell pellets were further processed

using the FITC Annexin V Apoptosis Detection Kit (BD Pharmingen™) according to the manufacturer's protocol by fluorescent activated cell sorter (FACS) analysis (BD FACSVerse, NJ, USA) (Bhatnagar et al., 2014).

2.9. Photoacoustic tomography

The noninvasive PAI system has been developed and described by Bui (Bui et al., 2015). In the present study, we modified the system to use only the pumping light (532 nm pump source, 10 Hz repetition rate, and 3–5 ns pulse width) from the Q-switched pulsed Nd:YAG laser (Surelite III, Continuum, CA, USA). The free-space output laser beam was coupled with a 0.22 -NA, 600-μm of core diameter multi-mode optical fiber (Thorlabs, NJ, USA) with a plano–convex lens of 50-mm focal length (Thorlabs). The output end of the fiber was combined with a 10-MHz single element, focused transducer (Panametrics, MA, USA) and aligned such that the center of the irradiated light would locate at the focal point of the transducer. The output end of the fiber and transducer were mounted on a three-dimensional (3D) linear actuator and moved for raster scanning. Output signals from the US transducer were amplified using an ultrasound pulser/receiver (5900 PR, Olympus, MA, USA). The signals were then digitized and stored using a data acquisition (DAQ) system, which includes a 100 -MS/s DAQ card (PXI-5122, National Instruments, TX, USA) and an embedded controller (PXI-1042Q, National Instruments). The trigger signals from the laser system were synchronized with the DAQ system to capture photoacoustic signals when the pulsed laser irradiated the sample. Both the DAQ system and the actuator were controlled by a custom-made LabView program. To form a photoacoustic image, the acquired photoacoustic signals were post-processed to improve image quality by applying a bandpass filter (3–20 MHz) to reduce noise. The Hilbert transform was used to detect the signal envelope by taking the absolute values of analytical signals. Finally, envelope signals were used to construct 3D photoacoustic image using a home-made Matlab program.

2.9.1. PTX-COS AuNPs labeling of MDA-MB-231 cells

Cells (3×10^5 cells/well) were treated with an IC_{50} concentration (220 μg/mL) of PTX-COS AuNPs and incubated for 24 h at 37 °C.
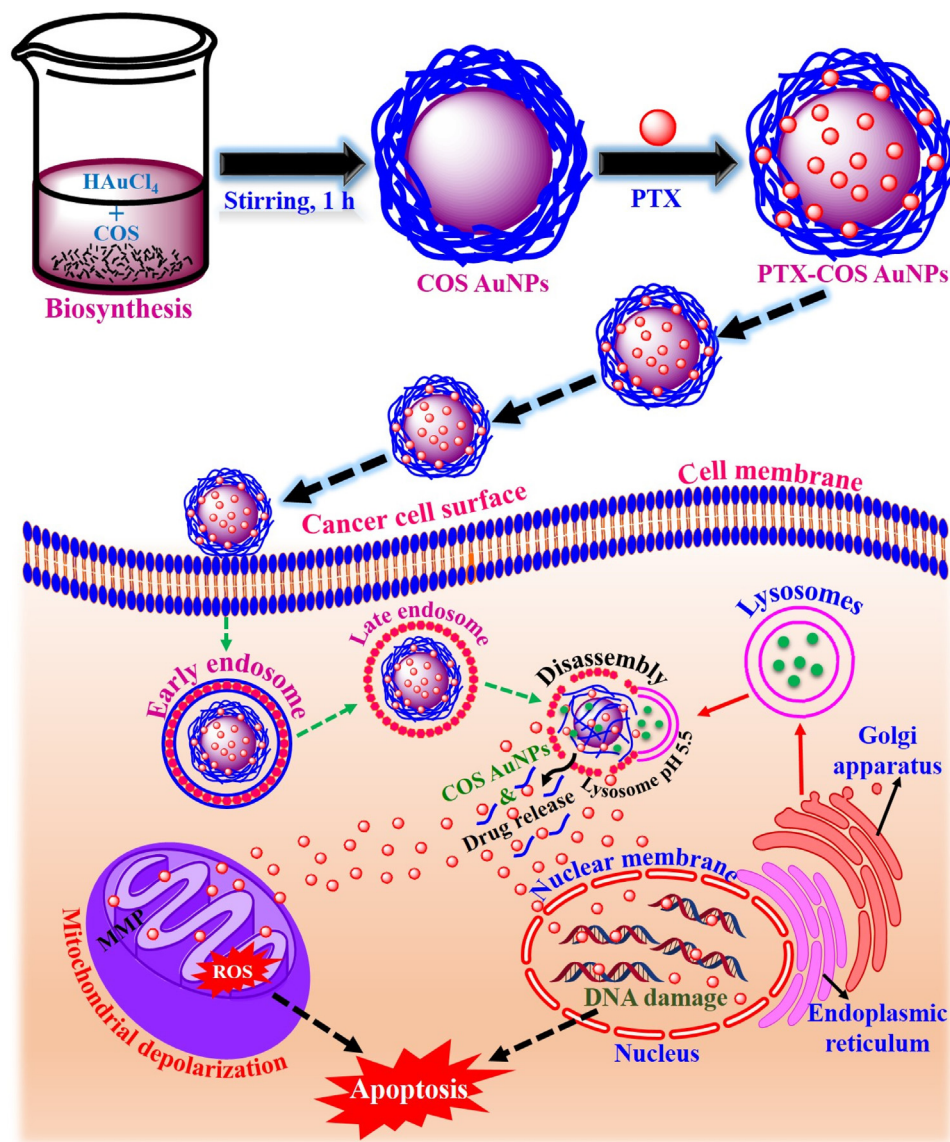
Scheme 1. Overall scheme for the biosynthesis of gold nanoparticles using chitosan oligosaccharide, subsequent loading of paclitaxel (PTX) on chitosan oligosaccharide-stabilized gold nanoparticles (COS AuNPs) and the possible mechanism for cellular uptake of paclitaxel-loaded chitosan oligosaccharide-stabilized gold nanoparticles (PTX-COS AuNPs) in MDA-MB-231 cancer cells.

Untreated cells (3×10^5 cells) were used as a control. After 24 h, the cells were washed with $1 \times$ PBS, and the morphological alterations in the cells were detected under a Leica DMI3000 B inverted phase contrast microscope. Treated and untreated cells were harvested and fixed with 4% formalin for 10 min. The cells were washed with $1 \times$ PBS, centrifuged at 1500 rpm for 3 min, and used for PAI.

2.9.2. Tissue-mimicking polyvinyl alcohol phantom

Polyvinyl alcohol (PVA) phantoms for imaging were constructed using 8% PVA (Sigma–Aldrich, St. Louis, USA), 0.4% silica (Min-U-Sil, U.S silica, Pacific, MO, USA) and 100 mL distilled water. Untreated cells and PTX-COS AuNPs- labeled MDA-MB-231 cells were included in the tissue-mimicking PVA phantom (Bui et al., 2015). Untreated cells and PTX-COS AuNPs- labeled MDA-MB-231 cells were mixed with 10% gelatin and used for two inclusions (50 μL each/well) in the tissue-mimicking PVA phantom. Using a micropipette, untreated and PTX-COS AuNPs- labeled MDA-MB-231 cells were poured into each well on PVA phantoms. The gelatin solution was used to cover inclusions after solidification. The PVA phantom was placed in the water tank of the PAI system to obtain images.

2.10. Statistical analysis

All the data were collected at least three times and were presented as mean ± standard deviation (SD). Statistical analysis was performed using one-way ANOVA by SPSS 14.

3. Results and discussion

COS is the degraded product of CS, which has been produced by several methods, including enzymatic and acidic hydrolysis. Recently, COS has received considerable attention in the food, biomedical, and chemical industries (Manivasagan and Oh, 2016). In the present study, COS was used considering its low-cost, water-soluble, biocompatible, biodegradable and nontoxic nature. COS was used as a reducing as well as stabilizing agent for the biosynthesis of AuNPs. Further, these biosynthesized AuNPs enabled the attachment of biological macromolecules (such as COS) and were subsequently loaded with PTX to demonstrate their use in anticancer drug delivery and PAI of cancer cells (Scheme 1).

3.1. Synthesis and characterization of COS AuNPs and PTX-COS AuNPs

First, the COS AuNPs were observed by visual observation in terms of appearance of color change in the reaction mixture. A clear ruby red color was formed within 1 h, which indicated the green synthesis of AuNPs, and the reaction mixture was examined by UV–vis spectroscopy. The reaction mixture was scanned in the range from 400 to 1100 nm. In the UV–vis absorption spectrum, a high peak at 537 nm was recorded, which is attributed to the SPR band of AuNPs (Fig. 1a).

FTIR spectroscopy was used to identify the possible biological macromolecules responsible for the bioreduction and stabilization of nanoparticles, which can help in their further functionalization
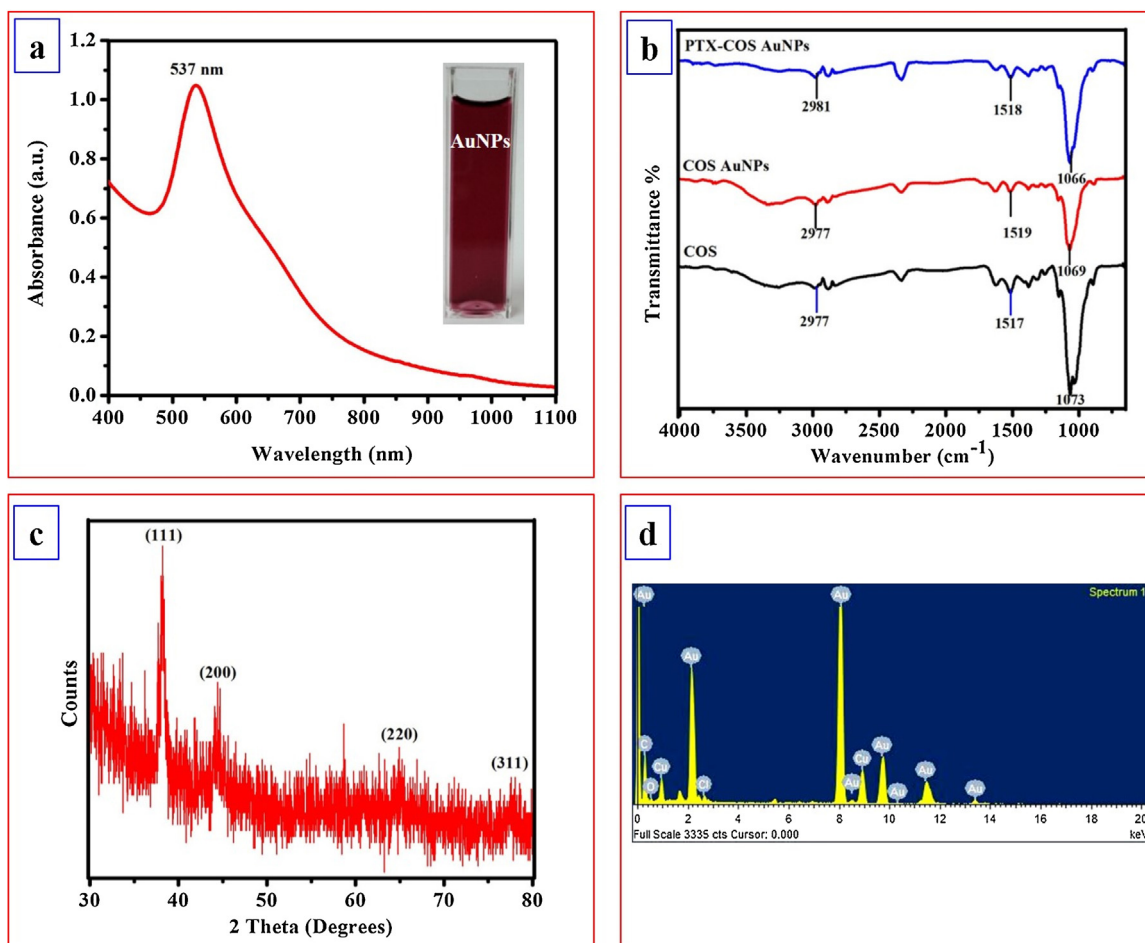

Fig. 1. (a) UV-vis spectra of chitosan oligosaccharide-stabilized gold nanoparticles. (b) FTIR spectroscopy of chitosan oligosaccharide (COS), chitosan oligosaccharide-stabilized gold nanoparticles (COS AuNPs) and paclitaxel-loaded chitosan oligosaccharide-stabilized gold nanoparticles (PTX-COS AuNPs). (c) XRD spectrum of chitosan oligosaccharide-stabilized gold nanoparticles. (d) EDX spectrum of chitosan oligosaccharide-stabilized gold nanoparticles.

with other compounds for several applications (Suvith and Philip, 2014). The FTIR spectrum of COS, COS AuNPs, and PTX-COS AuNPs showed bands at $1073\,cm^{-1}$, $1069\,cm^{-1}$, $1066\,cm^{-1}$, $1517\,cm^{-1}$, $1519\,cm^{-1}$, $1518\,cm^{-1}$, $2977\,cm^{-1}$, $2977\,cm^{-1}$, and $2981\,cm^{-1}$ (Fig. 1b). The medium bands detected at $1073\,cm^{-1}$, $1069\,cm^{-1}$, and $1066\,cm^{-1}$ in the spectra of COS, COS AuNPs, and PTX-COS AuNPs correspond to the C—N stretching of aliphatic amines. The strong bands observed at $1517\,cm^{-1}$, $1519\,cm^{-1}$, and $1518\,cm^{-1}$ were assigned to the N—O asymmetric stretching of nitro compounds. The medium bands at $2977\,cm^{-1}$, $2977\,cm^{-1}$, and $2981\,cm^{-1}$ correspond to the C—H stretching of alkanes.

The XRD pattern compared with the standard confirmed the spectrum of gold particles. The present study displayed nanocrystals as proven by the peaks at 2θ values of 38.23°, 44.58°, 64.89°, and 77.81° corresponding to (111), (200), (220), and (311) facets, respectively of the cubic crystalline structure. Fig. 1c clearly displays the characteristic diffraction peaks associated with crystalline gold. Manivasagan et al. (2015) have studied the XRD pattern of biosynthesized AuNPs corresponding to (111), (200),

(220), and (311) of cubic crystalline metallic gold. The FESEM image showed the spherical morphology of COS AuNPs equally distributed throughout the colloidal solution. The EDX spectrum of nanoparticles showed the highest peak at 8 keV for COS AuNPs (Fig. 1d). In addition, other peaks corresponding to C and O were observed due to unreacted precursors of gold solution. Interaction with Cu may emerge because of the grid used for analysis, and Cl peaks may occur because of the biomolecules bound to the surface of COS AuNPs.

HRTEM analysis was performed to determine the surface morphology of the COS AuNPs and PTX-COS AuNPs. Our HRTEM micrograph (Fig. 2a) clearly displays the spherical shape of the COS AuNPs with a size distribution from 23 to 101 nm having mean value of 60.64 ± 3.94 nm. Fig. 2b shows the HRTEM image of spherical PTX-COS AuNPs. The selected area electron diffraction pattern (SAED) showed four rings of Brag's reflections corresponding to the face-centered cubic (fcc) nature of crystalline COS AuNPs and PTX-COS AuNPs. The particle size analysis confirmed the distribution of COS AuNPs in the reaction mixture in terms of
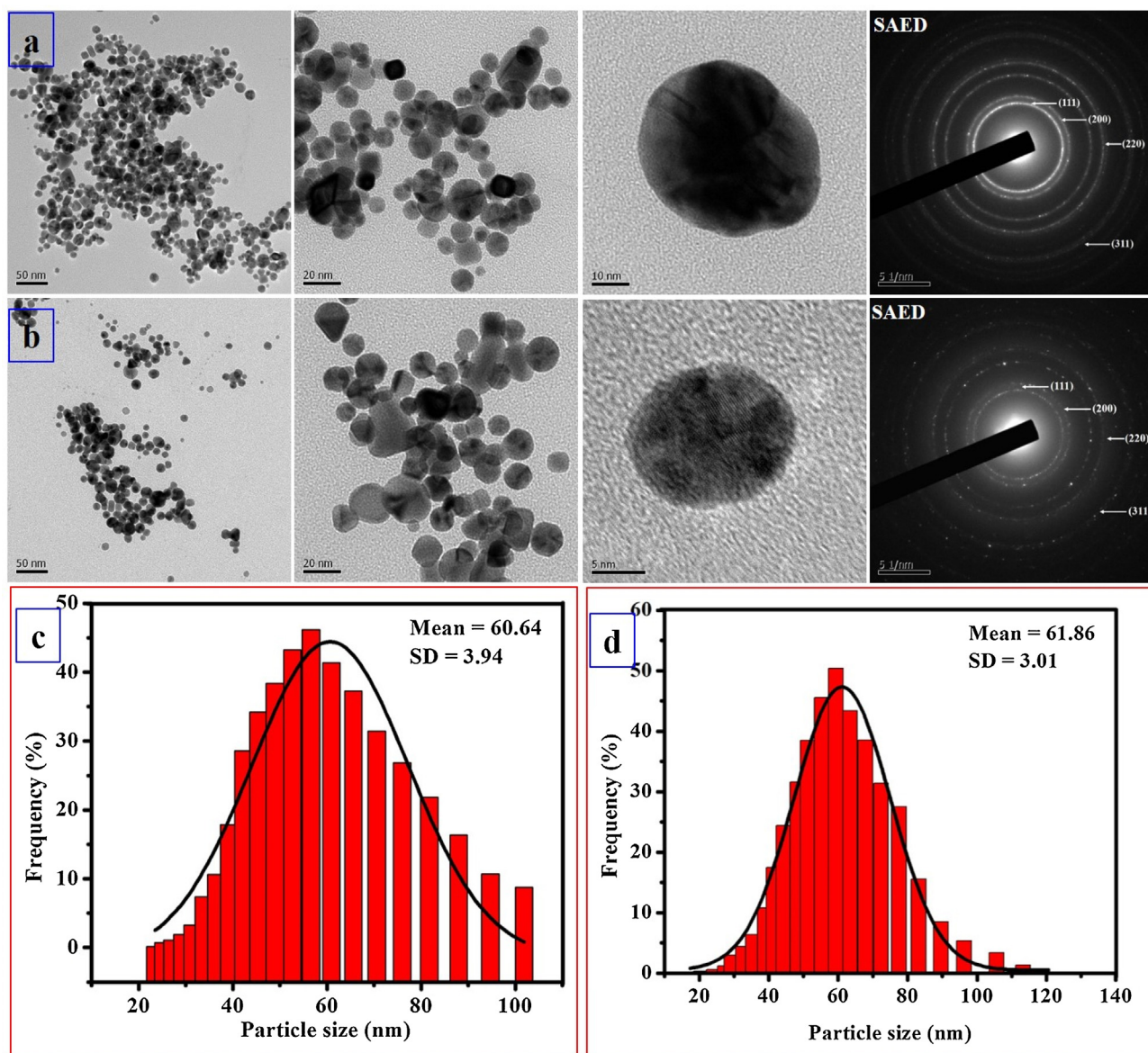

Fig. 2. (a) HRTEM micrograph and selected area electron diffraction pattern (SAED) of chitosan oligosaccharide-stabilized gold nanoparticles. (b) HRTEM micrograph and selected area electron diffraction pattern (SAED) of paclitaxel-loaded chitosan oligosaccharide-stabilized gold nanoparticles. DLS histogram of chitosan oligosaccharide-stabilized gold nanoparticles (c) and paclitaxel-loaded chitosan oligosaccharide-stabilized gold nanoparticles (d).

intensity, number, and volume of nanoparticles. The frequency distribution recorded from the histogram displayed that almost 90% COS AuNPs were in the 42–76 nm size range. These results are in agreement with the values obtained by DLS measurement as shown in Fig. 2c. The hydrodynamic particle size of PTX-COS AuNPs was 61.86 ± 3.01 nm as measured by DLS (Fig. 2d). Surface ZP is one of the important parameters for characterizing the stability of nanoparticles in the aqueous environment. For COS AuNPs and PTX-COS AuNPs, the ZP value was found to be +13.85 mV and +13.10 mV, respectively. This proves the stability and positive surface charge of the COS AuNPs. The positive charge could be attributed to the presence of protonated amino groups of COS. In the case of PTX-COS AuNPs, there was a slight decrease in ZP resulting from the interaction of electropositive groups of the polysaccharide with the electronegative group of PTX.

3.2. Stability study of COS AuNPs

The stability of COS AuNPs is most important in biomedical and therapeutic applications. Therefore, the *in vitro* stability of COS AuNPs was investigated in different month intervals (Fig. 3a), various pH (Fig. 3b), and different concentrations of NaCl (Fig. 3c). There was no visible variation in the UV–vis spectrum of the COS AuNPs solution even after six months, which revealed the highly stable nature of the COS AuNPs. The size of COS AuNPs after six months was 59.52 ± 2.61 nm as measured by DLS (Fig. 3d). The effect of pH change in the range of 2.0–12.0 on the stability of COS AuNPs was studied. The results revealed, no observable change in the wavelength recorded, which further confirmed the stable nature of COS AuNPs. In addition, the stability was observed at various concentration of NaCl (10^1 to 10^5 M). These nanoparticles did not show any major change in peak intensity indicating their high stability. Thus, these results revealed the high stability of COS AuNPs under different month intervals, various pH, and different concentrations of NaCl, which will help in the effective application of COS AuNPs in biomedical field.

3.3. Preparation of PTX-COS AuNPs

After the successful biosynthesis of highly stable COS AuNPs, we have visualized this system for anticancer drug delivery and PAI through subsequent loading of biological macromolecules. We had chosen an anticancer drug PTX for loading COS AuNPs. PTX could be easily loaded into COS AuNPs during the formation of nanoparticles by a dialysis technique with a DL efficiency of 82.71% and DCs of 4.34%. Therefore, COS AuNPs are predicted to be
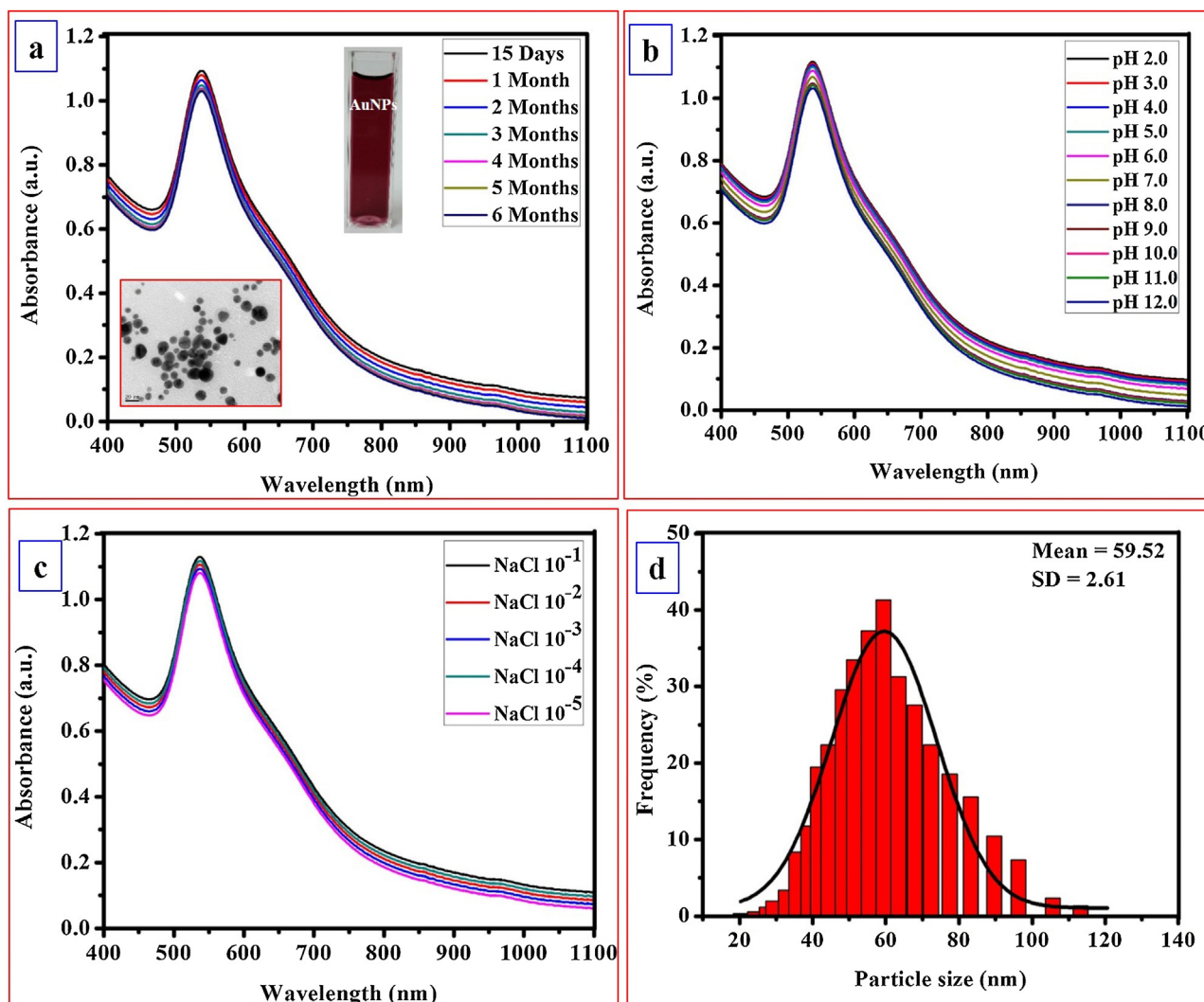

Fig. 3. UV-vis spectra of chitosan oligosaccharide-stabilized gold nanoparticles of six months stability study (a) (inset showed HRTEM image o six months stability sample of COS AuNPs) at various pH conditions (b) and different concentration of NaCl (c). (d) DLS histogram of chitosan oligosaccharide-stabilized gold nanoparticles of six months stability study.

promising drug carriers for the delivery of PTX in combination chemotherapy.

3.4. In vitro drug release

The capacity of the carrier to efficiently release the cargo at the desired site is a main feature of any delivery vehicles. PTX release pattern from COS AuNPs was studied under various pH conditions (5.5, 6.8 and 7.5) at 37 °C (Fig. 4a). PTX release from the COS AuNPs was observed for 48 h. Sustained drug release was detected and it was dependent on the pH of the release medium. Approximately 19% PTX was released in the first 3 h under all pH conditions. After that, the amounts of PTX released from COS AuNPs increased as the pH value of the releasing medium decreased. After 48 h, 96% PTX was completely released at pH 5.5 and 68% and 56% PTX was released at pH 6.8 and 7.4, respectively. These results indicated that the release of PTX was higher in acidic pH than in neutral pH. This pH-dependent release may increase the efficiency of PTX as the uptake of drug-loaded nanoparticles through endocytosis process leads to exposure to an acidic environment (Bareford and Swaan, 2007) and the subsequent release would ultimately result in improved cytotoxic effect against breast cancer cells.

3.5. In vitro cytotoxicity studies

For the successful application of nanomaterials in biomedicine field, it is very important to check their potential cytotoxicity. The cytotoxicity of COS, COS AuNPs, PTX, and PTX-COS AuNPs were tested on MDA-MB-231 cells using MTT assay. Figs. 4b and c show the plot of cell viability against various concentrations of COS, COS AuNPs, PTX, and PTX-COS AuNPs for 24 h and 48 h. They exhibited dose-dependent cytotoxicity. The IC_{50} value of COS, COS AuNPs, PTX, and PTX-COS AuNPs against MDA-MB-231 was 300 μg/mL, 280 μg/mL, 200 μg/mL, and 220 μg/mL, respectively after 24 h, whereas it was 300 μg/mL, 260 μg/mL, 220 μg/mL, and 240 μg/mL, respectively after 48 h. The cytotoxicity of PTX-COS AuNPs was lower than that of COS and COS AuNPs, which clearly indicated the excellent anticancer effect of PTX-COS AuNPs against MDA-MB-231 cells.

3.5.1. Morphological observations

PTX-COS AuNPs induced several morphological changes in MDA-MB-231 cells after 24 h and 48 h incubation, however, no observable changes were seen in untreated cells (Fig. 5a). The PTX-COS AuNPs stimulated various morphological changes including cell clumping, cell communication inhibition, cell shape alterations, and chromatin condensation in MDA-MB-231 cells, which underwent cell death, whereas the untreated cells were active. PTX-COS AuNPs activated the apoptosis pathway through the generation of ROS and, alteration of MMP in MDA-MB-231 cells, leading to cell death.

3.5.2. Apoptosis study

The induction of apoptosis, after the treatment with IC_{50} concentration of PTX-COS AuNPs, was evaluated by fluorescence microscopy after staining with AO/EB. The stained cells were
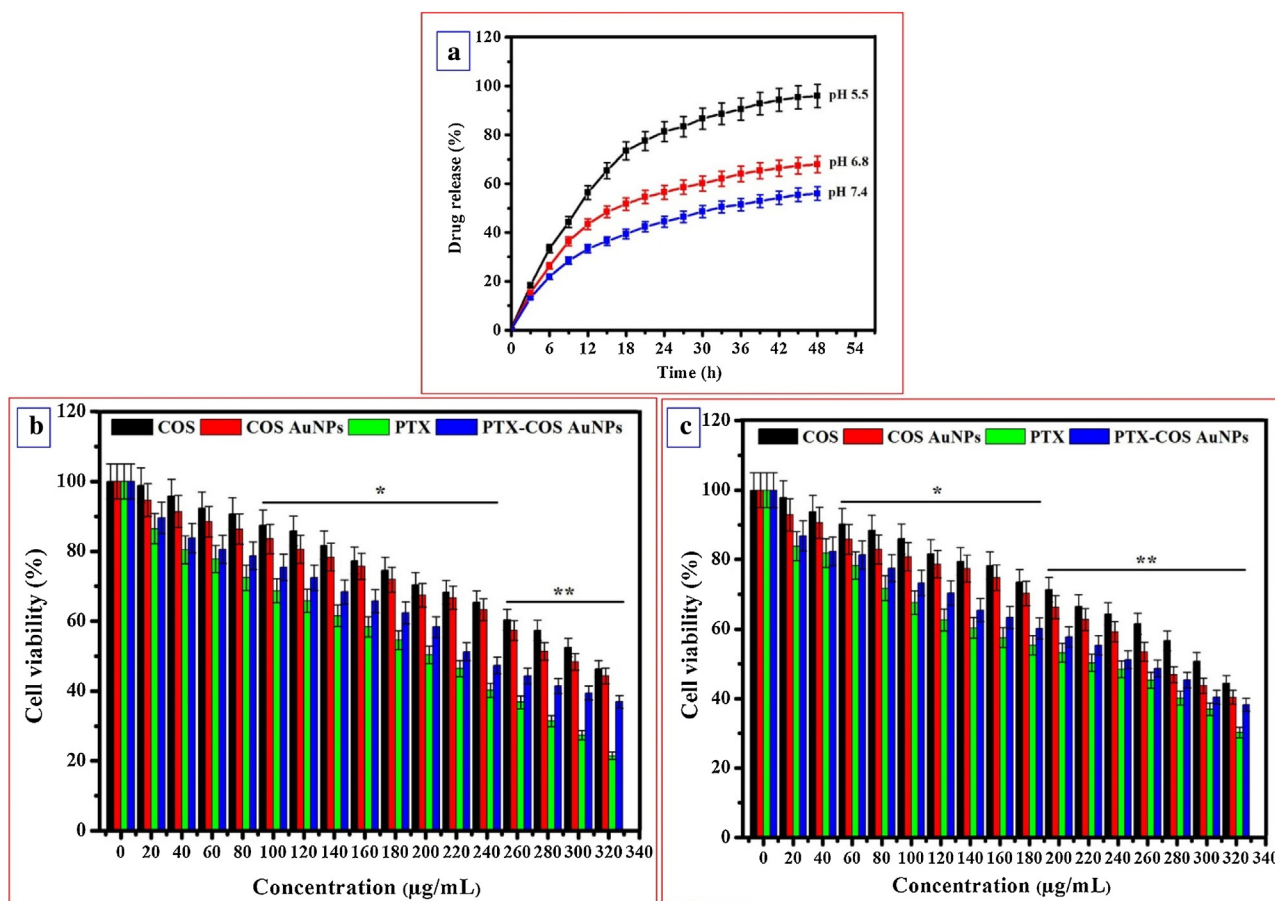

Fig. 4. (a) *In vitro* PTX release profile from paclitaxel-loaded chitosan oligosaccharide-stabilized gold nanoparticles. Date is expressed as mean ± SD of the three experiments. *In vitro* cytotoxic effect of chitosan oligosaccharide (COS), chitosan oligosaccharide-stabilized gold nanoparticles (COS AuNPs), paclitaxel (PTX) and paclitaxel-loaded chitosan oligosaccharide-stabilized gold nanoparticles (PTX-COS AuNPs) against MDA-MB-231 cells for 24 h (b) and 48 h (c), respectively. Data is expressed as mean ± SD of the three experiments. Percentage of cytotoxicity is expressed relative to untreated controls (* significant $p < 0.05$; ** highly significant $p < 0.01$).
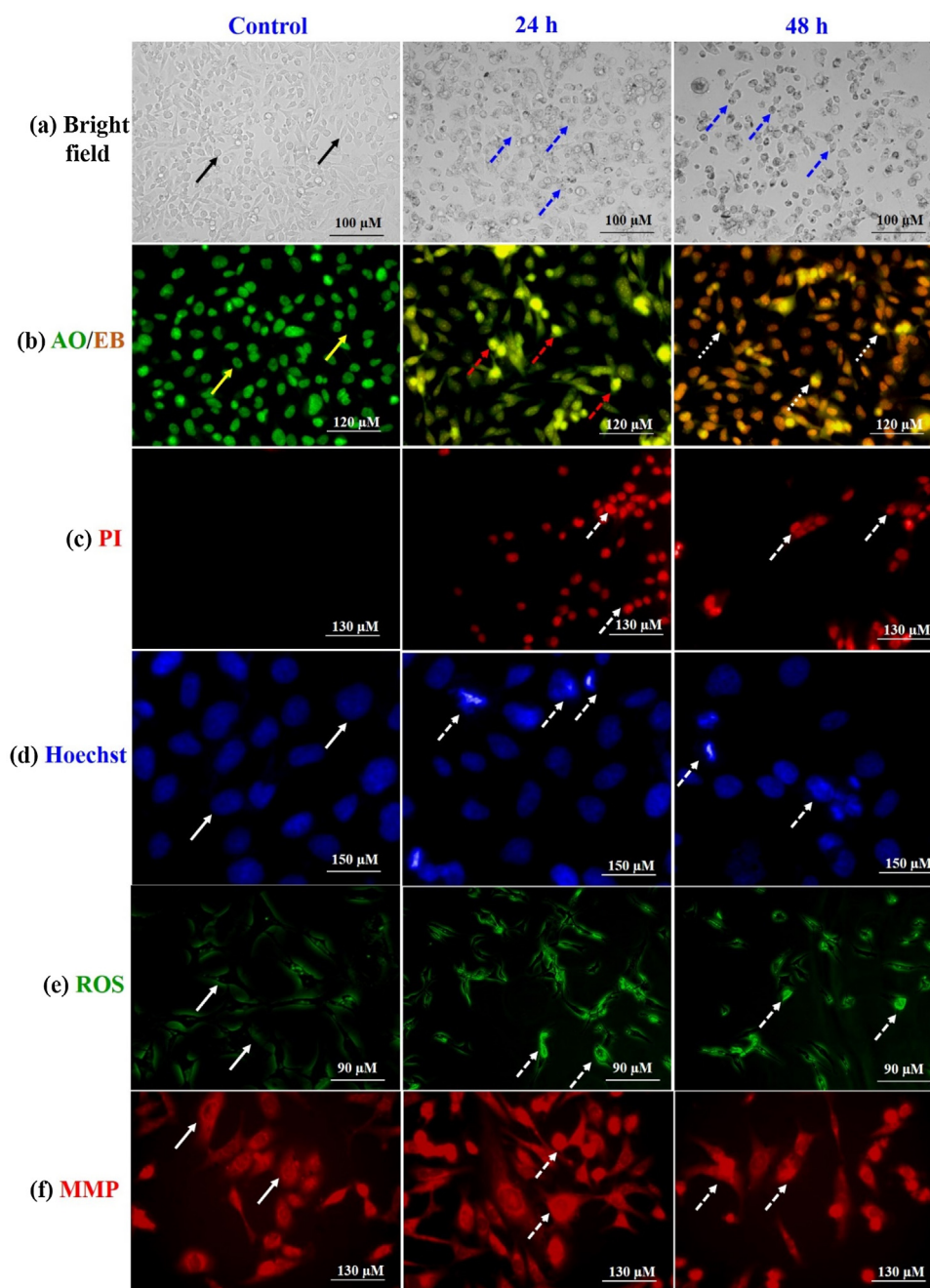
Fig. 5. (a) Morphological changes in MDA-MB-231 cells incubated with IC_{50} concentration (220 μg/mL and 240 μg/mL) of paclitaxel-loaded chitosan oligosaccharide-stabilized gold nanoparticles for 24 h and 48 h, as assessed by contrast phase microscopy (20× magnification). (b) Acridine orange/ethidium bromide (AO/EB) staining of MDA-MB-231 cells in control and treated with IC_{50} concentration of paclitaxel-loaded chitosan oligosaccharide-stabilized gold nanoparticles for 24 h and 48 h, as assessed by fluorescence microscopy (40 × magnification). (c) Propidium iodide staining of MDA-MB-231 cells in control and treated with IC_{50} concentration of paclitaxel-loaded chitosan oligosaccharide-stabilized gold nanoparticles for 24 and 48 h as assessed by fluorescence microscopy (40× magnification). (d) Hoechst 33342 staining of MDA-MB-231 cells in control and treated with IC_{50} concentration of paclitaxel-loaded chitosan oligosaccharide-stabilized gold nanoparticles for 24 and 48 h as assessed by fluorescence microscopy (40× magnification). (e) Intracellular reactive oxygen species level in the MDA-MB-231 cells in control and treated with IC_{50} concentration of paclitaxel-loaded chitosan oligosaccharide-stabilized gold nanoparticles for 24 and 48 h as assessed by fluorescence microscopy (20× magnification). (f) Mitochondrial membrane potential level in the MDA-MB-231 cells in control and treated with IC_{50} concentration of paclitaxel-loaded chitosan oligosaccharide-stabilized gold nanoparticles for 24 and 48 h as assessed by fluorescence microscopy (40× magnification).

characterized as viable (green fluorescence), early apoptotic (yellow fluorescence and condensed chromatin), late apoptotic (orange fluorescence), and nonviable cells (red colored fluorescence) (Fig. 5b). AO can penetrate the normal cell membrane and hence, the cells exhibited green fluorescence. In apoptotic cells, apoptotic bodies formed as result of chromatin condensation, membrane blebbing and fragmentation of nuclei were observed as yellow and orange colored bodies whereas, necrotic cells exhibited red color fluorescence because of their loss of membrane integrity.

Fig. 5c shows the apoptotic cell stained with PI. The cells treated with an IC_{50} concentration of PTX-COS AuNPs showed increased number of apoptotic alterations and nuclear condensation. In the case of control cells, very few PI positive cells were observed, which clearly indicated that PTX-COS AuNPs could induce cell

death in MDA-MB-231 through ROS-mediated apoptotic process. The increased ROS levels and subsequent loss of MMP might be the reason for the increase apoptotic in morphological alterations in PTX-COS AuNPs treated cells (Piao et al., 2011).

In Hoechst 33342 staining, after the treatment with IC_{50} concentration of PTX-COS AuNPs for 24 h and 48 h, MDA-MB-231 cells commence to show apoptotic characteristics, including chromatin condensation, cell shrinkage, and fragmentation, whereas the untreated cells showed normal nuclei (Fig. 5d). These morphological alterations are due to the activation of caspase cascades, which cleave the specific substrates responsible for the DNA repair activation. This result clearly indicates that the PTX-COS AuNPs could induce cell death through apoptosis.
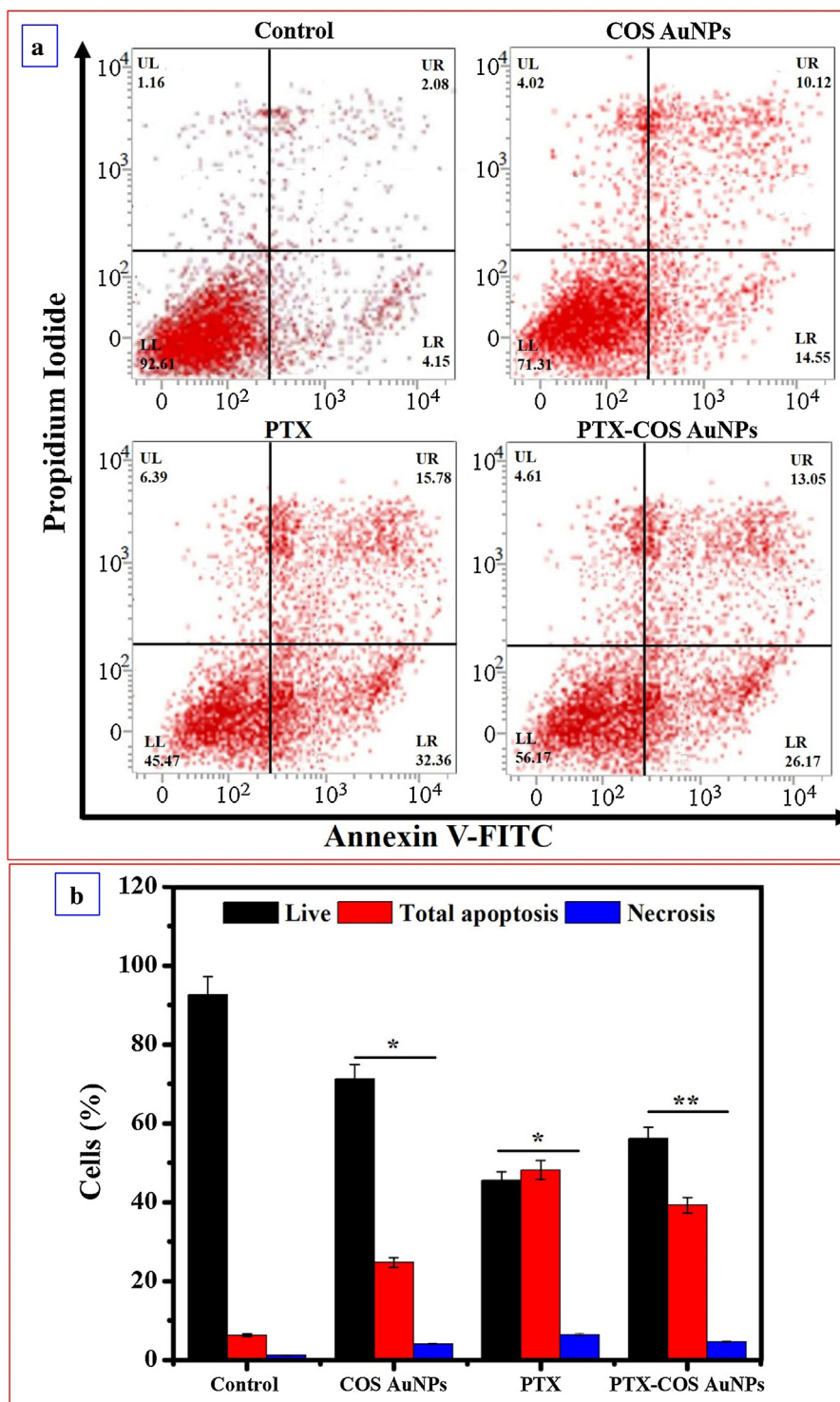

Fig. 6. (a) Fluorescence-activated cell sorting (FACS) analysis of apoptosis in MDA-MB-231 cells incubated with 220 μg/mL of chitosan oligosaccharide-stabilized gold nanoparticles (COS AuNPs), paclitaxel (PTX), and paclitaxel-loaded chitosan oligosaccharide-stabilized gold nanoparticles (PTX-COS AuNPs) measured using fluorescein isothiocyanate (FITC)-labeled Annexin V and PI. Representative dot plots showing the distribution of Annexin V and PI staining for control, COS AuNPs, PTX, and PTX-COS AuNPs-treated cells. (b) Bar graph represents the mean percentages of apoptosis and necrosis (* significant $p < 0.05$; (** highly significant $p < 0.01$).

3.5.3. Reactive oxygen species (ROS) detection

In recent years, many reports have shown that ROS can play an important role in anticancer activities (Wan et al., 2013). Numerous anticancer drugs are known to show their activity by generating intracellular ROS (Velayutham et al., 2005). To study the effect of PTX-COS AuNPs on intracellular ROS generation, DCHF-DA was used as a fluorescent probe. The fluorescence microscopy analysis showed that IC_{50} concentration of PTX-COS AuNPs produced bright green fluorescence in treated cells, indicating the generation of ROS, whereas the control cells did not exhibit any fluorescence (Fig. 5e). These results indicated that PTX-COS AuNPs increased the levels of ROS.

3.5.4. Mitochondrial membrane potential

Mitochondria is thought to be the main pathway for apoptosis, and, therefore, targeting them is a new approach fin cancer therapy (He et al., 2013). The changes in the MMP were determined by fluorescence microscope. It is well known that during apoptosis the MMP decreases. The effect of PTX-COS AuNPs on MMP was assessed in MDA-MB-231 cells. The cells were exposed to IC_{50} concentration of PTX-COS AuNPs for 24 h and 48 h and assayed for Rh-123 uptake using fluorescence microscope (Fig. 5f). The fluorescent intensity was reduced in cells exposed to PTX-COS AuNPs, which clearly indicated a significant reduction of MMP in MDA-MB-231 cells.

3.6. Cell cycle analysis

Apoptosis and cell cycle arrest are associated with anticancer activity in cancer cells. The cell death caused by COS AuNPs, PTX and PTX-COS AuNPs were reconfirmed by apoptosis assay in MDA-MB-231 cells using flow cytometry. Fig. 6a represents the apoptotic profile of MDA-MB-231 cells, where the X and Y-axis show the Annexin V-FITC and PI emissions respectively. MDA-MB-231 cells were treated with COS AuNPs, PTX and PTX-COS AuNPs at concentrations of 220 μg/mL for 24 h. PTX-COS AuNPs induced both early and late apoptosis in a concentration-dependent manner compared with untreated control cells. The percentage of apoptosis observed was 6.23%, 24.67%, 48.14%, and 39.22% in control, COS AuNPs, PTX, and PTX-COS AuNPs-treated MDA-MB-231 cells, which strongly indicated the induction of apoptosis (Fig. 6b).

3.7. Photoacoustic imaging

Fig. 7a and b shows the 3D and the top view of the tissue-mimicking PVA phantom including one inclusion of untreated cells (control) and 220 μg/mL PTX-COS AuNPs-labeled MDA-MB-231 cells. The maximum intensity projection (MIP) image along the z-axis to xy plane of the phantom (Fig. 7c) is displayed over a 14 mm × 6 mm field of view. It clearly reveals the distribution of PTX-COS AuNPs labeled MDA-MB-231 cells inside the phantom. The high-amplitude photoacoustic signals could not be detected in untreated cells (control), which did not have PTX-COS AuNPs. The high-amplitude photoacoustic signals were detected from inclusions of PTX-COS AuNPs-labeled MDA-MB-231 cells. The incident light homogeneously distributed over the volume of inclusions containing PTX-COS AuNPs-labeled MDA-MB-231 cells because of the optical scattering inside the cells. Fig. 7d shows the 3D photoacoustic image of the phantom with the 14 mm × 6 mm × 3 mm field of view. Biological targeting of PTX-COS AuNPs to cancer cells may further increase the magnitude or change the pattern of PTX-COS AuNPs accumulation inside cancer cells. This could be well studied using PAI as demonstrated here. The ability to image PTX-COS AuNPs inside cancer cells with PAI also suggests an opportunity for image-guided cancer therapy, with PTX-COS AuNPs serving as cancer imaging contrast agents and mediators of cancer therapy. The presently employed laser system (532 nm) for PAT, used in conjunction with PTX-COS AuNPs as a novel contrast agent, has the potential to allow for non-invasive early
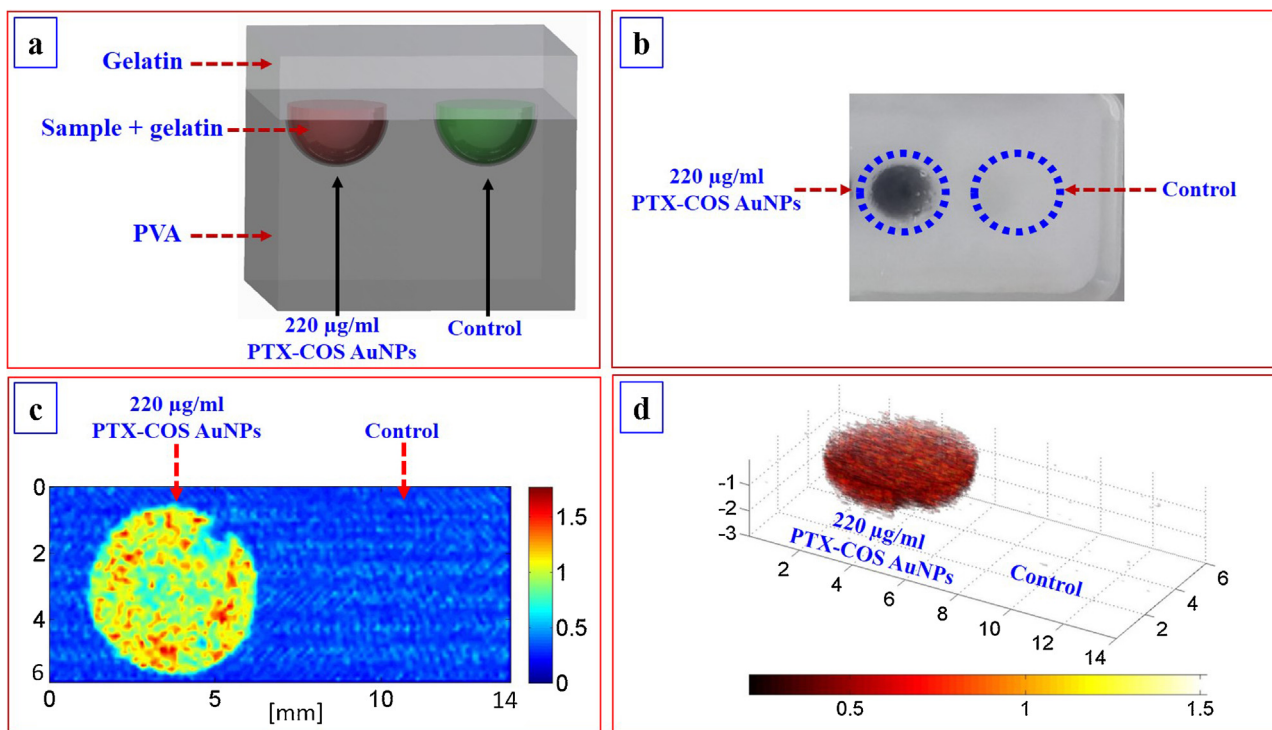

Fig. 7. (a) Three dimensional (3D) diagram of tissue mimicking polyvinyl alcohol phantom. (b) Diagram of tissue mimicking polyvinyl alcohol phantom shows a top view structure. (c) Photoacoustic image of untreated cells (control) and 220 μg/mL of PTX-COS AuNPs labeled MDA-MB-231 cells. (d) Three dimensional (3D) photoacoustic image of untreated cells (control) and 220 μg/mL of PTX-COS AuNPs labeled MDA-MB-231 cells.

diagnosis and image-guided treatment of superficial, often refractory, tumors such as breast cancer, malignant melanoma, and Mekel cell carcinoma (Zhang et al., 2009). Zhong et al. (2015) reported the high efficient photoacoustic treatment using gold nanorods and its antitumor activity. Gold nanorods can produce much stronger shock waves and induce the efficient cancer cell death, which strongly indicated the gold nanorods as multifunctional probes for imaging-guided photoacoustic tumor therapy. Zhong et al. (2016) reported the paclitaxel-containing nanoparticles as a novel drug delivery system and photoacoustic imaging. Paclitaxel (PTX), perfluorohexane (PFH) and gold nanorods (AuNRs) loaded nanoparticles (PTX-PAnP) were synthesized. Folic acid (FA) conjugated PTX-PAnP (PTX-PAnP-FA) could be selectively taken into folate receptor-overexpressed tumor cells. The PTX-PAnP-FA nanoparticles can facilitate multiple mechanisms, including bubble implosion, shockwave generation and sonoporation that further enhance the therapeutic efficiency. It provides an all-in-one platform for photoacoustic image-guided drug release and synergistic chemo-photoacoustic therapy.

4. Conclusion

The potential of nanobiotechnology in the biomedical field of anticancer therapeutics has been clearly recognized. In the present study, we have successfully synthesized PTX-COS AuNPs as novel agents for drug delivery and PAI of cancer cells. This simple procedure appears to be suitable for large-scale production as it is efficient, fast, cost-effective, eco-friendly, and safe for clinical research. We designed and biosynthesized AuNPs using COS as reducing and stabilizing agent and characterized using XRD, FTIR, FESEM, HRTEM, SAED, EDX, DLS and ZP. The biosynthesized COS AuNPs were spherical with an average particle size of 60.64 ± 3.94 nm. The PTX-COS AuNPs exhibited strong cytotoxic effects against MDA-MB-231 cells through the induction of apoptosis with enhanced ROS generation and altered MMP level. Fluorescence microscopy and flow cytometry studies showed that PTX-COS AuNPs exhibited excellent cellular uptake in MDA-MB-231 cells. PTX-COS AuNPs were also developed as a new class of optical contrast agent for photoacoustic medical imaging. To the best of our knowledge, no previous studies described the use of PTX-COS AuNPs as novel agents for drug delivery and PAI of cancer cells. This study suggests that PTX-COS AuNPs can be used as novel anticancer agents for breast cancer treatment and can have potential as a novel class of contrast agents for PAI, thus advancing the future prospects of nanotechnology in the pharmaceutical industry.

Acknowledgement

References

Agnihotri, S.A., Mallikarjuna, N.N., Aminabhavi, T.M., 2004. Recent advances on chitosan-based micro-and nanoparticles in drug delivery. J. Control. Release. 100, 5–28.

Bareford, L.M., Swaan, P.W., 2007. Endocytic mechanisms for targeted drug delivery. Adv. Drug Deliver. Rev. 59, 748–758.

Bhatnagar, I., Venkatesan, J., Kim, S.-K., 2014. Polymer functionalized single walled carbon nanotubes mediated drug delivery of gliotoxin in cancer cells. J. Biomed. Nanotechnol. 10, 120–130.

Bhosle, S.M., Huilgol, N.G., Mishra, K.P., 2005. Enhancement of radiation-induced oxidative stress and cytotoxicity in tumor cells by ellagic acid. Clin. Chim. Acta 359, 89–100.

Bui, N.Q., Hlaing, K.K., Nguyen, V.P., Nguyen, T.H., Oh, Y.-O., Fan, X.F., Lee, Y.W., Nam, S.Y., Kang, H.W., Oh, J., 2015. Intravascular ultrasonic-photoacoustic (IVUP)

endoscope with 2. 2-mm diameter catheter for medical imaging. Comput. Med. Imag. Graph. 45, 57–62.

Chae, S.Y., Son, S., Lee, M., Jang, M.-K., Nah, J.-W., 2005. Deoxycholic acid-conjugated chitosan oligosaccharide nanoparticles for efficient gene carrier. J. Control. Release. 109, 330–344.

Choi, J.-S., Seo, K., Yoo, J.-W., 2012. Recent advances in PLGA particulate systems for drug delivery. J. Pharm. Invest. 42, 155–163.

De Volder, M.F., Tawfick, S.H., Baughman, R.H., Hart, A.J., 2013. Carbon nanotubes: present and future commercial applications. Science 339, 535–539.

Dhand, V., Soumya, L., Bharadwaj, S., Chakra, S., Bhatt, D., Sreedhar, B., 2016. Green synthesis of silver nanoparticles using *Coffea arabica* seed extract and its antibacterial activity. Mater. Sci. Eng. C 58, 36–43.

He, N., Shi, X., Zhao, Y., Tian, L., Wang, D., Yang, X., 2013. Inhibitory effects and molecular mechanisms of selenium-containing tea polysaccharides on human breast cancer MCF-7 cells. J. Agric. Food Chem. 61, 579–588.

Heister, E., Neves, V., Tîlmaciu, C., Lipert, K., Beltrán, V.S., Coley, H.M., Silva, S.R.P., McFadden, J., 2009. Triple functionalisation of single-walled carbon nanotubes with doxorubicin, a monoclonal antibody, and a fluorescent marker for targeted cancer therapy. Carbon 47, 2152–2160.

Hsieh, T.-c., Wijeratne, E.K., Liang, J.-y., Gunatilaka, A.L., Wu, J.M., 2005. Differential control of growth, cell cycle progression, and expression of NF-κB in human breast cancer cells MCF-7, MCF-10A, and MDA-MB-231 by ponicidin and oridonin, diterpenoids from the chinese herb *Rabdosia rubescens*. Biochem. Bioph. Res. Co. 337, 224–231.

Hu, F.-Q., Meng, P., Dai, Y.-Q., Du, Y.-Z., You, J., Wei, X.-H., Yuan, H., 2008. PEGylated chitosan-based polymer micelle as an intracellular delivery carrier for anti-tumor targeting therapy. Eur. J. Pharm. Biopharm. 70, 749–757.

Huang, X., Jain, P.K., El-Sayed, I.H., El-Sayed, M.A., 2007. Gold nanoparticles: interesting optical properties and recent applications in cancer diagnostics and therapy. Future Nanomed. 2, 681–693.

Jabr-Milane, L.S., van Vlerken, L.E., Yadav, S., Amiji, M.M., 2008. Multi-functional nanocarriers to overcome tumor drug resistance. Cancer Treat. Rev. 34, 592–602.

Karthik, S., Sankar, R., Varunkumar, K., Ravikumar, V., 2014. Romidepsin induces cell cycle arrest, apoptosis, histone hyperacetylation and reduces matrix metalloproteinases 2 and 9 expression in bortezomib sensitized non-small cell lung cancer cells. Biomed. Pharmacother. 68, 327–334.

Krishnaraj, C., Muthukumaran, P., Ramachandran, R., Balakumaran, M., Kalaichelvan, P., 2014. *Acalypha indica* Linn: biogenic synthesis of silver and gold nanoparticles and their cytotoxic effects against MDA-MB-231, human breast cancer cells. Biotechnol. Reports 4, 42–49.

Kruss, S., Hilmer, A.J., Zhang, J., Reuel, N.F., Mu, B., Strano, M.S., 2013. Carbon nanotubes as optical biomedical sensors. Adv. Drug Deliv. Rev. 65, 1933–1950.

Kumar, M.R., Muzzarelli, R.A., Muzzarelli, C., Sashiwa, H., Domb, A., 2004. Chitosan chemistry and pharmaceutical perspectives. Chem. Rev. 104, 6017–6084.

Lee, E., Lee, J., Lee, I.-H., Yu, M., Kim, H., Chae, S.Y., Jon, S., 2008. Conjugated chitosan as a novel platform for oral delivery of paclitaxel. J. Med. Chem. 51, 6442–6449.

Liu, Z., Jiao, Y., Wang, Y., Zhou, C., Zhang, Z., 2008. Polysaccharides-based nanoparticles as drug delivery systems. Adv. Drug Deliv. Rev. 60, 1650–1662.

Liu, Z., Robinson, J.T., Tabakman, S.M., Yang, K., Dai, H., 2011. Carbon materials for drug delivery & cancer therapy. Mater. Today 14, 316–323.

Manivasagan, P., Oh, J., 2016. Marine polysaccharide-based nanomaterials as a novel source of nanobiotechnological applications. Int. J. Biol. Macromol. 82, 315–327.

Manivasagan, P., Alam, M.S., Kang, K.-H., Kwak, M., Kim, S.-K., 2015. Extracellular synthesis of gold bionanoparticles by *Nocardiopsis* sp. and evaluation of its antimicrobial, antioxidant and cytotoxic activities. Bioprocess Biosyst. Eng. 38, 1167–1177.

Manivasagan, P., Nam, S.Y., Oh, J., 2016. Marine microorganisms as potential biofactories for synthesis of metallic nanoparticles. Crit. Rev. Microbiol. 1–13. doi:http://dx.doi.org/10.3109/1040841X.1042015.1137860.

Nagajyothi, P., Muthuraman, P., Sreekanth, T., Kim, D.H., Shim, J., 2016. Green synthesis: in-vitro anticancer activity of copper oxide nanoparticles against human cervical carcinoma cells. Arab. J. Chem. doi:http://dx.doi.org/10.1016/j.arabjc.2016.01.011.

Piao, M.J., Kang, K.A., Lee, I.K., Kim, H.S., Kim, S., Choi, J.Y., Choi, J., Hyun, J.W., 2011. Silver nanoparticles induce oxidative cell damage in human liver cells through inhibition of reduced glutathione and induction of mitochondria-involved apoptosis. Toxicol. Lett. 201, 92–100.

Singh, P., Singh, H., Kim, Y.J., Mathiyalagan, R., Wang, C., Yang, D.C., 2016. Extracellular synthesis of silver and gold nanoparticles by *Sporosarcina koreensis* DC4 and their biological applications. Enzyme Microb. Technol. 86, 75–83.

Suvith, V., Philip, D., 2014. Catalytic degradation of methylene blue using biosynthesized gold and silver nanoparticles. Spectrochim. Acta Part A 118, 526–532.

Tagad, C.K., Dugasani, S.R., Aiyer, R., Park, S., Kulkarni, A., Sabharwal, S., 2013. Green synthesis of silver nanoparticles and their application for the development of optical fiber based hydrogen peroxide sensor. Sens. Actuat. B-Chem. 183, 144–149.

Tai, K.-W., Chou, M.-Y., Hu, C.-C., Yang, J.-J., Chang, Y.-C., 2000. Induction of apoptosis in KB cells by pingyangmycin. Oral Oncol. 36, 242–247.

Tao, Y., Han, J., Dou, H., 2012. Paclitaxel-loaded tocopheryl succinate-conjugated chitosan oligosaccharide nanoparticles for synergistic chemotherapy. J. Mater. Chem. 22, 8930–8937.

Velayutham, M., Villamena, F.A., Fishbein, J.C., Zweier, J.L., 2005. Cancer chemopreventive oltipraz generates superoxide anion radical. Arch. Biochem. Biophys. 435, 83–88.

Venkatpurwar, V., Shiras, A., Pokharkar, V., 2011. Porphyran capped gold nanoparticles as a novel carrier for delivery of anticancer drug: *in vitro* cytotoxicity study. Int. J. Pharm. 409, 314–320.

Wan, J., Liu, T., Mei, L., Li, J., Gong, K., Yu, C., Li, W., 2013. Synergistic antitumour activity of sorafenib in combination with tetrandrine is mediated by reactive oxygen species (ROS)/Akt signaling. Br. J. Cancer 109, 342–350.

Xiong, J., Meng, F., Wang, C., Cheng, R., Liu, Z., Zhong, Z., 2011. Folate-conjugated crosslinked biodegradable micelles for receptor-mediated delivery of paclitaxel. J. Mater. Chem. 21, 5786–5794.

Xue, M., Hu, S., Lu, Y., Zhang, Y., Jiang, X., An, S., Guo, Y., Zhou, X., Hou, H., Jiang, C., 2015. Development of chitosan nanoparticles as drug delivery system for a prototype capsid inhibitor. Int. J. Pharm. 495, 771–782.

Zhang, X., Li, Y., Chen, X., Wang, X., Xu, X., Liang, Q., Hu, J., Jing, X., 2005. Synthesis and characterization of the paclitaxel/MPEG-PLA block copolymer conjugate. Biomaterials 26, 2121–2128.

Zhang, C., Qu, G., Sun, Y., Wu, X., Yao, Z., Guo, Q., Ding, Q., Yuan, S., Shen, Z., Ping, Q., 2008. Pharmacokinetics, biodistribution, efficacy and safety of N-octyl-O-sulfate chitosan micelles loaded with paclitaxel. Biomaterials 29, 1233–1241.

Zhang, Q., Iwakuma, N., Sharma, P., Moudgil, B., Wu, C., McNeill, J., Jiang, H., Grobmyer, S., 2009. Gold nanoparticles as a contrast agent for in vivo tumor imaging with photoacoustic tomography. Nanotechnology 20, 1–8.

Zhong, J., Wen, L., Yang, S., Xiang, L., Chen, Q., Xing, D., 2015. Imaging-guided high-efficient photoacoustic tumor therapy with targeting gold nanorods. Nanomed. Nanotechnol. Biol. Med. 11, 1499–1509.

Zhong, J., Yang, S., Wen, L., Xing, D., 2016. Imaging-guided photoacoustic drug release and synergistic chemo-photoacoustic therapy with paclitaxel-containing nanoparticles. J. Control. Release 226, 77–87.